Nov 15 2022 08:12 am

Water Loss — 11%

Electrolyte Loss — 18%

pH Level — 4 5 6 7 8 — 5.4

RESEARCH ARTICLE

EcoMat FUNCTIONAL MATERIALS FOR GREEN ENERGY AND ENVIRONMENT **WILEY**

Soft, environmentally degradable microfluidic devices for measurement of sweat rate and total sweat loss and for colorimetric analysis of sweat biomarkers

Shanliangzi Liu[1] | Da Som Yang[1] | Shaotang Wang[1] | Haiwen Luan[1] | Yurina Sekine[2] | Jeffrey B. Model[1,3] | Alexander J. Aranyosi[1,3] | Roozbeh Ghaffari[1,3,4] | John A. Rogers[1,4,5,6,7,8,9]

[1]Querrey Simpson Institute for Bioelectronics, Northwestern University, Evanston, Illinois, USA

[2]Materials Sciences Research Center, Japan Atomic Energy Agency, Tokai, Japan

[3]Epicore Biosystems, Inc., Cambridge, Massachusetts, USA

[4]Department of Biomedical Engineering, Northwestern University, Evanston, Illinois, USA

[5]Department of Materials Science and Engineering, Northwestern University, Evanston, Illinois, USA

[6]Department of Mechanical Engineering, Northwestern University, Evanston, Illinois, USA

[7]Department of Neurological Surgery, Northwestern University, Evanston, Illinois, USA

[8]Department of Electrical and Computer Engineering, Northwestern University, Evanston, Illinois, USA

[9]Department of Chemistry, Northwestern University, Evanston, Illinois, USA

Correspondence
John A. Rogers, Querrey Simpson Institute for Bioelectronics, Northwestern University, Evanston, IL, USA.
Email: jrogers@northwestern.edu

Abstract

Advanced capabilities in noninvasive, in situ monitoring of parameters related to sweat serve as the basis for obtaining real-time insights into human physiological state, health, and performance. Although recently reported classes of soft, skin-interfaced microfluidic systems support powerful functions in this context, most are designed as single-use disposables. As a result, associated waste streams have the potential to create adverse environmental impacts. Here, we introduce materials and fabrication techniques that bypass these concerns through biodegradable microfluidic systems with a full range of features, including measurement of sweat rate and total loss, and colorimetric analysis of biomarkers. The key components fully degrade through the enzymatic action of microorganisms in natural soil environments, or in industrial compost facilities, to yield end products with beneficial uses as fertilizers and species to improve soil health. Detailed characterization of the constituent materials, the fabrication procedures, the assembly processes, and the completed devices reveal a set of essential performance parameters that are comparable to, or even better than, those of non-degradable counterparts. Human subject studies illustrate the ability of these devices to acquire

accurate measurements of sweat loss, sweat rate, pH, and chloride concentration during physical activities and thermal exposures.

KEYWORDS

biodegradable, colorimetric, microfluidics, sweat

1 | INTRODUCTION

Recent advances in materials and device designs form the foundations for soft, low-modulus, and thin wearable devices that directly interface with human skin for medical diagnosis and human physiological performance monitoring.[1] As a relatively underexplored biofluid for biomedical evaluations, sweat is particularly interesting for its rich range of chemical constituents including electrolytes, metabolites, organic compounds, hormones, and proteins and for its capability for noninvasive collection.[2] Emerging classes of skin-mounted devices exploit some combination of soft microfluidic structures, electronic components, and chemical sensors to enable real-time assessments of physiological health via the measurements of sweat loss, sweat rate, and biomarker concentrations.[3]

Previously reported 'skin-like', sometimes referred to as 'epidermal', microfluidic systems rely primarily on polydimethylsiloxane (PDMS), a silicone elastomer, as the main constituent material because of its excellent biocompatibility, chemical stability, gas permeability, optical transparency, skin-compatible mechanical properties, and ease of fabrication via the methods of soft lithography.[4,5] These devices typically serve as single-use platforms, due to practical considerations in cleaning and sterilization for re-use. Although silicones are non-toxic, their covalently cross-linked structures and their high levels of chemical and thermal stability yield highly inert, non-biodegradable materials that can remain in the environment for decades or hundreds of years.[6] Recently launched commercial devices rely on other classes of non-biodegradable materials, also in a single-use format.[7] As a result, an emerging concern is in proper management of waste streams created by discarded devices. The development of alternative, biocompatible and biodegradable materials and suitable fabrication methods for soft microfluidic systems are, therefore, of high interest.

The following introduces materials, fabrication approaches, and assembly techniques for soft, microfluidic systems that can fully biodegrade naturally in the soil or in industrial composting facilities to yield environmentally beneficial end products. The materials and methods are distinct from those in related platforms reported recently, thereby providing engineering schemes to achieve systems with biodegradation capabilities that can be applied in not only microfluidics but also other skin-interfaced wearable systems. Demonstration vehicles support capabilities for in situ sweat capture, storage, and biomarker analysis, with performance characteristics comparable to those of non-degradable counterparts.[8–10] Detailed studies encompass key material characteristics, including mechanical, chemical, optical, and thermal properties, and the associated methods for forming high-precision microfluidic structures in ways that align with large-scale manufacturing practice in preparation for future mass production of consumer products. Trials with human subjects illustrate use in practical scenarios.

2 | RESULTS AND DISCUSSION

2.1 | Soft, environmentally degradable microfluidic devices for measurement of sweat rate and total loss and for colorimetric analysis of biomarkers

The microfluidic device platform relies almost entirely (>90% by mass) on a set of constituent materials that are fully degradable through the enzymatic action of microorganisms, in a manner aligned with commercial industrial compostability standards (EN 13432), within 90 days to leave no visible or toxic residues. The materials can also biodegrade in natural soil environments, at rates that depend on the microorganism population, temperature, humidity, pH and other factors. In all cases, unlike more standard polymeric microfluidic and injection molded devices, the end products of this degradation process are CO_2, water and biomass, with potential uses as soil nutrients and energy sources. The following uses the term biodegradable to encompass natural processes as well as those in industrial composting facilities.

The resulting devices are soft and thin, capable of gently conforming to the skin, as an interface for capture, storage, and sensing of biomarkers in sweat. Inlets on the skin-facing side of the device allow sweat, as it emerges from the surface of the skin, to flow into a sealed collection of microchannels, microvalves, and microreservoirs that enable assessments of sweat rate and total sweat loss and, in the examples described in the following, that
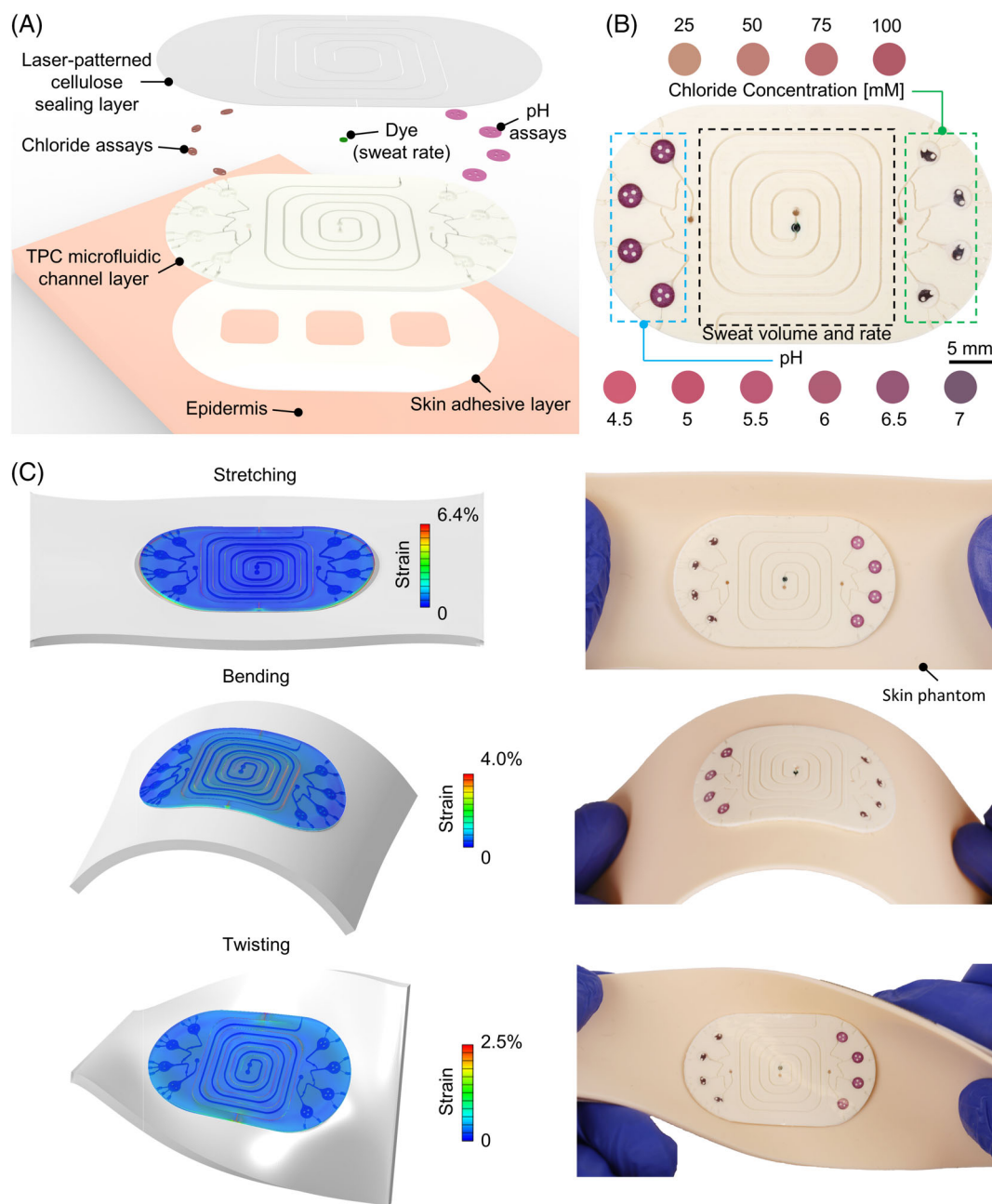
FIGURE 1 Soft, environmentally biodegradable microfluidic devices for sweat capture, storage and biomarker analysis. (A) Exploded view schematic illustration of the key layers and components of a representative device. TPC: thermoplastic copolyester elastomer. (B) Optical image of a device that includes a microfluidic channel for sweat volume and rate measurement, and reservoirs with colorimetric assays for pH and chloride analysis. The color evolution of both assays occurs over physiologically relevant ranges of chloride and pH in human sweat. (C) Finite element analysis results and respective optical images of the devices on silicone skin phantoms during stretching (25%), bending (radius of curvature 35 mm), and twisting (90°)

support colorimetric chemical assays for determining the pH and concentration of chloride in the collected sweat (Figure 1A). The key advance reported here is in the use of constituent materials and assays that are biodegradable and the development of suitable fabrication techniques that can serve as a versatile solution to other wearable systems with biodegradability demands, aligned with large-scale manufacturing practice for future mass production.

The microfluidic layer consists of a low-modulus thermoplastic copolyester elastomer (∼5.3 MPa) patterned through a multi-step molding process. This layer bonds to a transparent film of cellulose via an acrylic pressure-sensitive adhesive to seal and encapsulate the system.

Laser structuring this thin (∼90 μm), high-modulus (∼1.75 GPa) film into an open but interconnected geometry reduces the bending stiffness and elastic modulus of the completed device. The result allows significant levels of flexibility and stretchability to enable a conformal, non-irritating and water-tight interface to the skin with a thin (∼150 μm), low modulus (∼17 kPa) dual-sided adhesive. Sweat passes from defined collection areas (∼60 mm^2) into the microchannels through the action of natural pressure generated by eccrine sweat glands.

Choices of microfluidic designs and material geometries consider various factors, including the volume of sweat that can be collected, the mechanical stability of the microchannels and microreservoirs against mechanical collapse and the system-level mechanics of the completed device. The devices reported here exploit microfluidic layers with thicknesses of ∼750 μm and microchannels/microreservoirs/microvalves with depths of ∼330 μm. An independent, serpentine microchannel in the middle of the device allows monitoring of sweat rate and loss up to a volume of ∼20 μl. As shown in Figure 1B, green food dye near the inlet facilitates visual evaluation of the extent of filling of this microchannel with sweat during use. The dye consists primarily of chlorophyll, which degrades after use into colorless, non-fluorescent chlorophyll catabolites via a bio-metabolism process, leaving no toxic intermediates.[11–13] Two additional sets of microchannels and microreservoirs support measurements of the pH and the concentration of chloride in sweat via colorimetric chemical assays. Digital image processing techniques allow for quantitation.

Unlike pH assays that use various hazardous chemicals,[8] the systems reported here rely on anthocyanin, a natural indicator extracted from red cabbage. Degradation occurs through the action of enzymes such as β-glucosidase, polyphenol-oxidase, and peroxidase, which are produced by microorganisms, to yield various phenolic acids, amino acids, proteins, and other quinones.[13–15] This indicator is unique in its combination of good sensitivity, reversibility, biodegradability, and proven compatibility with other analytes that can be found in sweat.[16] The chloride assay uses the reagent silver chloranilate, dispersed in polyhydroxyethyl methacrylate (pHEMA) methanolic suspension. PHEMA is a highly biocompatible hydrogel that is widely used in biomedical applications,[17] degradable by macrophage cell lines.[18] Copolymerizing HEMA with different methacrylates or reducing the molecular weight both enhance the degradability.[17] Silver chloranilate is not biodegradable, but it is non-toxic and is commonly used in environmental-friendly analytical procedures for spectrophotometric determination of chloride.[19] As silver chloranilate only makes up 0.03 wt% of the constituent materials, its effects on the biodegradability of the entire system are minimal because this percentage lies well below criteria for compostability standards.[20] The demonstrated color

evolution in Figure 1B corresponds to physiologically relevant levels of chloride and pH in human sweat. Each of the reservoirs for pH and chloride detection has a capacity of ∼1.8 ± 0.1 μl. The circular posts in these reservoirs prevent mechanical collapse that might otherwise occur upon impact or application of pressure. Capillary bursting valves (CBVs) integrated into the microchannel network passively direct sweat through the system in a sequential fashion that enables chronometric sampling of sweat, as described previously.[21]

Finite element analysis (FEA, using mechanical properties of constituent materials described subsequently) of stress–strain distributions and associated photographs highlight the mechanical behaviors of devices bonded to silicone skin phantoms (2.5 mm-thick, 130 kPa) during stretching (25%), bending (radius of curvature 35 mm), and twisting (90°) (Figure 1C). These deformations significantly exceed those in most practical scenarios for use, including those described subsequently. The color scale corresponds to strain distributions over the device area, except for narrow strain concentrations in the thermoplastic elastomer layer that occur near the patterned slits of the cellulose layer (results with full color scale appear in Figure S1, Supporting Information). Under these mechanical distortions, the maximum principal strains are ∼0.4% and ∼18% for the cellulose and thermoplastic elastomer, respectively. The peak interfacial stresses at the surface of the skin phantom reach 20 kPa, approximately equal to the sensory perception threshold of human skin (Figure S2, Supporting Information).[10,22]

2.2 | Materials selection and fabrication

The constituent materials for biodegradable microfluidic devices must satisfy a range of requirements for mechanical, chemical, optical, and thermal properties, as well as for process compatibility and mass manufacturability. Ideal candidates for the microfluidic layer constituents should possess the following key attributes: (1) chemistries to allow biodegradation in natural or industrial environments; (2) low elastic moduli to enable comfortable and reliable bonding to the skin; (3) high surface energy to ensure adhesive wetting and robust bonding to the sealing layer; (4) low water absorption and permeability to capture and store sweat without significant loss; (5) pure white color to serve as a reference background for accurate color analysis; (6) low processing temperatures to allow compatibility with soft lithography; (7) ease of fabrication and scalability to enable cost-effective mass production.

The field of bioresorbable electronics, as a subset of the broader area of transient electronics, relies on a range of materials for substrates and encapsulation layers, including silk fibroin,[23,24] wax,[25] collagen,[26] poly(lactic-
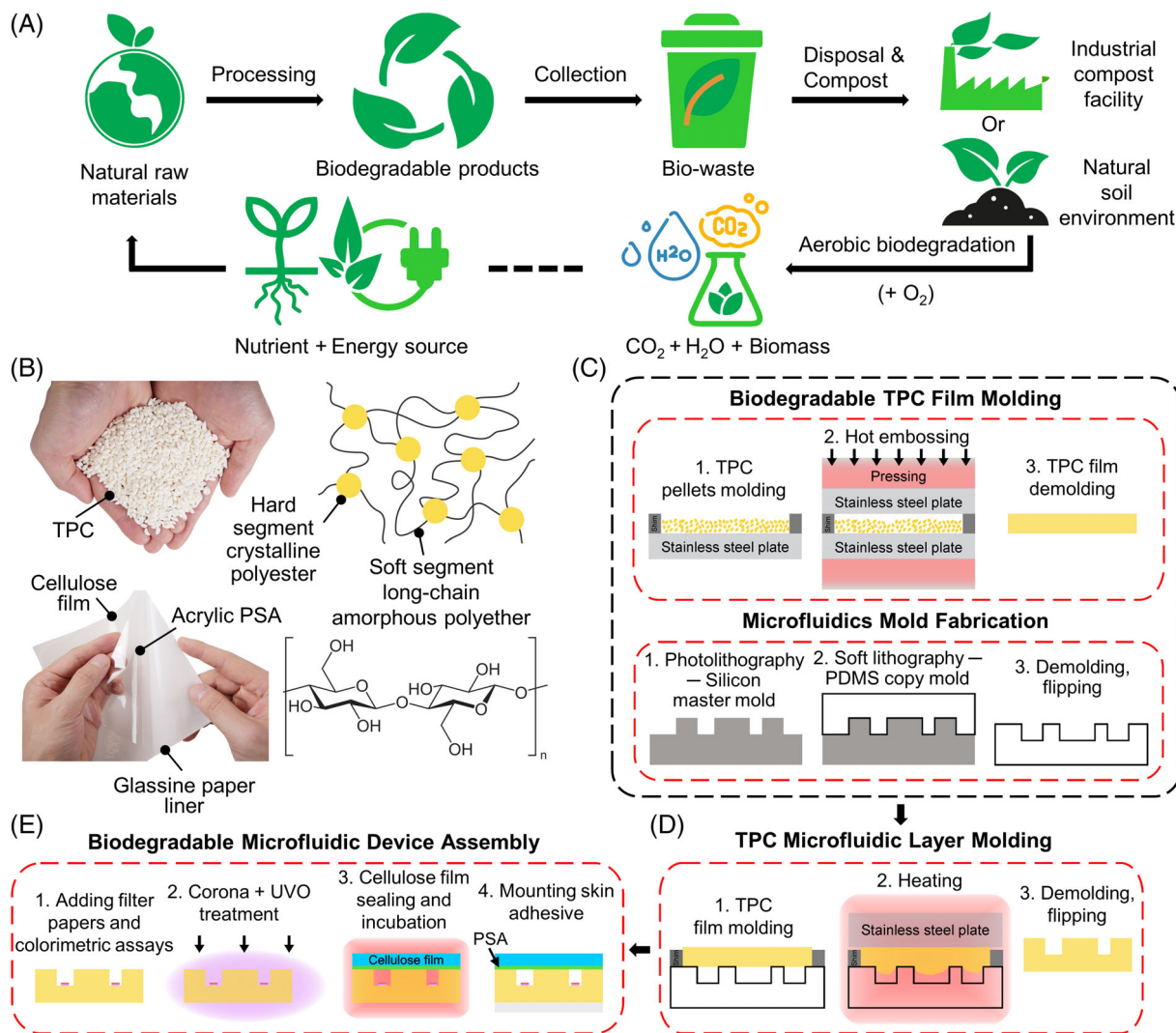
FIGURE 2 Material processing schemes, degradation mechanisms and fabrication methods. (A) Biodegradation process of biodegradable materials in natural soil environments, or in industrial compost facilities. (B) Pictures and chemical structures of a biodegradable thermoplastic copolyester elastomer (TPC) for the microfluidic layer and a cellulose film with an acrylic pressure-sensitive adhesive (PSA) for the sealing layer. (C–E) Illustration of the steps for device fabrication: (C) fabrication of a silicon master mold, a PDMS replica mold, and a molded TPC film; (D) fabrication of a TPC microfluidic layer; (E) assembly of a device by adding filter papers and colorimetric assays to the TPC microfluidic layer, bonding the cellulose sealing layer on top, and mounting onto a skin-compatible adhesive on the bottom

co-glycolic acid) (PLGA),[27,28] polyanhydride,[29] polycaprolactone (PCL),[30,31] and poly(1,8-octanediol-co-citrate) (POC).[32] Each of these materials dissolves completely and harmlessly by hydrolysis in biofluids within weeks or months, but none satisfies all of the requirements listed above and most are not currently in mass production. Alternatively, biodegradable materials for food packaging, textiles, consumer goods, and agriculture are in increasing demand.[20,33,34] Industrial composting facilities exploit microorganisms to decompose these materials into CO_2, water, and biomass, the latter of which can be used as a nutrient and energy source to produce natural raw products (Figure 2A). The most common

biodegradable materials available on a commercial scale include poly(lactic acid) (PLA), polyhydroxyalkanoate (PHA), starch blends, and polybutylene-based polymers, such as polybutylene succinate (PBS), polybutyrate-adipate-terephthalate (PBAT), and other synthetic polyesters.[35–41] Among these and other biodegradable materials, thermoplastic copolyester elastomers (TPCs), including the commercial APINAT™ BIO Biodegradable compounds (Trinseo), satisfy all of the requirements for the sweat microfluidic systems described here.[42] These polymers incorporate hard, crystalline polyester segments as thermally stable components, and soft, long-chain amorphous polyether segments that define the elastomeric

properties (Figure 2B). The labile ester bonds in these materials are susceptible to attack from enzymes excreted by microorganisms, yielding small molecules that can be absorbed by microbial cells and can be further utilized by the microorganisms in processes that depend on temperature and other factors.[43] Compounding the TPC material with small amounts of titanium dioxide-based white pigment yields a near-white color, without altering its biodegradability. Titanium dioxide is commonly used in paint, sunscreen, food coloring, and photocatalytic degradation of pollutants.[44,45] In the environment, titanium dioxide usually has low solubility and is stable once particle aggregates form in soil, but it can be consumed by microorganisms through trophic transfer.[46] The rates of degradation increase with dissolved organic matter and clay in the soil.[47]

The top sealing layer must be optically transparent to allow for visual and/or colorimetric assessments of sweat. Most biodegradable polymers involve crystalline components that strongly scatter light. An exception is cellulose (NatureFlex™ NVS film, FUTAMURA) as shown in Figure 2B. Cellulose originates from wood pulp sourced from harvested crops and wood. Enzymes from microorganisms, such as cellulases, can break down the β-1,4 glycosidic bonds in cellulose.[48,49] An acrylic pressure-sensitive adhesive (PSA, S9500, Avery Dennison) laminated onto the cellulose film bonds films of this material to the microfluidic layer to create a sealed microfluidic assembly. In the first phase of degradation of this PSA, side groups of the acrylic copolymers such as amide, nitrile, or alkyl groups bound by ester bonds cleave from the C—C backbone via hydrolytic enzymatic reactions produced by microorganisms. In the second phase, the C—C backbone breaks down through aerobic metabolism pathways.[50] The TPC, cellulose, and PSA all conform to the same commercial industrial compostability standard EN 13432 and can be degraded at industrial composting facilities within 90 days.

Figure 2C–E presents a schematic illustration of the process for molding the microfluidic layer of TPC. Melting TPC pellets on a stainless steel plate on the bottom platen of a hydraulic press, placing another stainless steel plate on top once the temperature reaches the set point at 160°C, then applying a 2 kN embossing force for 5 min by pressing the top platen, and finally releasing the force and cooling the assembly back to room temperature creates a film with thickness defined by a shim (Figure 2C). The microfluidic structures follow from embossing the surfaces of films produced in this manner using PDMS molds defined by casting and curing against a patterned silicon wafer (Figure 2C, D). Heating for 4 h at 160°C melts the film to facilitate flow into the features of relief on the PDMS, without significant applied pressure. A 0.5 mm-thick shim placed on the PDMS replica mold defines the thickness of the device. Data from

differential scanning calorimetry (DSC) of the TPC appear in Figure S3, Supporting Information.

Mechanically punching inlets in the resulting TPC microfluidic layer and placing filter papers and colorimetric assays into the microreservoirs prepare the device for the final assembly step (Figure 2E). Enhancing the surface energy of the TPC layer by exposing it to a corona discharge and UV induced ozone, and then laminating a film of cellulose with PSA (20 μm) on top and incubating at 75°C for 48 h forms a sealed microfluidic system. Mounting the assembled device onto a skin-compatible adhesive completes the fabrication process. Details appear in the Experimental Section.

2.3 | Characterization of biodegradable microfluidics

Figure 3 summarizes the results of various physical measurements of the constituent materials and the completed devices. The stress–strain behavior of a film of TPC (1 mm in thickness; Figure 3A, B) indicates a high strain to failure (∼600%), a low elastic modulus (∼5.3 MPa), and a yield strain of ∼18%. These features facilitate nondestructive demolding of delicate microfluidic structures during the fabrication process, support a comfortable interface to the skin, and allow for elastic recovery following deformations associated with wear. Stress–strain cycling tests at various peak strains indicate small mechanical hysteresis at low strains (<20%), and significant increases with increasing strain (Figure 3B). The cellulose film shows a strain to failure of ∼20%, a yield strain of 1.5%, and an elastic modulus of 1.75 GPa (Figure 3C).

Water uptake and barrier properties are important for collecting and storing sweat with minimized absorption and evaporative losses. Figure 3D indicates that the sweat absorption of TPC (∼2% by weight) is slightly lower than that of PDMS (∼2.5%).[8,51] The absorption of the cellulose films is ∼40% in 3.5 h, which is significantly larger than TPC and PDMS, but the overall effects are small due to the thin geometry of the sealing layer. The sweat absorption of these materials over 50 h appear as an inset. The cellulose film (∼45 μm) has a water vapor transmission rate (WVTR) of 113 g·mm/(m^2·day), which is ∼3.4 times lower than the WVTR of PDMS (382 g·mm/(m^2·day)).[52] Since the permeation rate decreases with film thickness,[53] evaporative losses during sweat capture and storage can be further reduced by stacking two films of cellulose to yield a bilayer with thickness of ∼90 μm. Details are in Figure S4, the Supporting Information, and the Experimental Section. The optical transparency of the bilayer is indistinguishable from that of the single layer (Figure 3E).
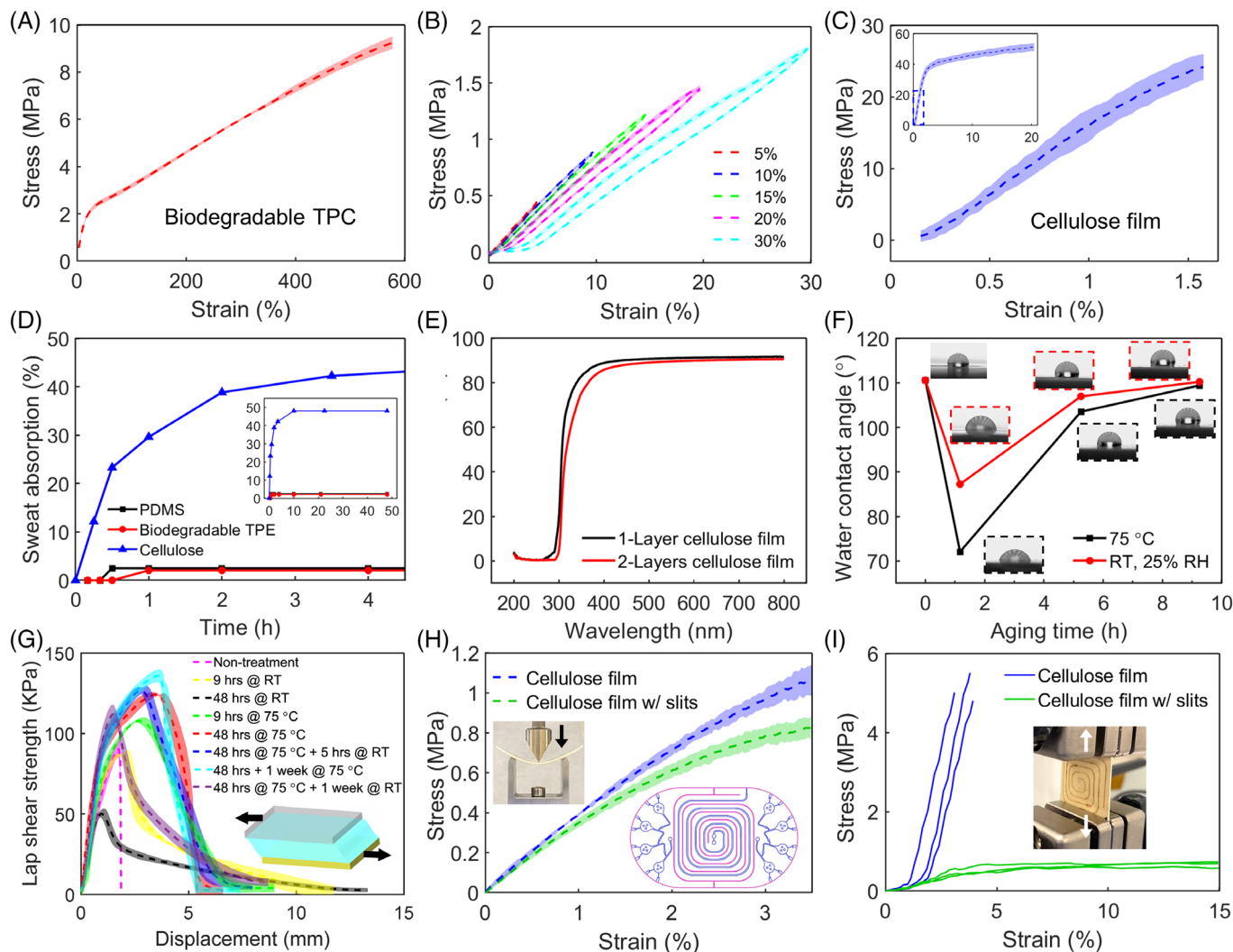
FIGURE 3 Characterization of biodegradable microfluidic systems constructed with TPC and cellulose. (A) The stress–strain behaviors of a sample of TPC during tensile tests. The shaded area represents a 95% confidence interval across five tests. (B) Stress–strain behaviors of similar samples across various strains (5%, 10%, 15%, 20%, and 30%). The shaded areas represent 95% confidence intervals across five cycles at each strain. (C) The stress–strain behavior of a sample of cellulose during tensile tests. The shaded area represents a 95% confidence interval across five tests. (D) The low water absorption of biodegradable TPC compared with PDMS enables stable sweat collection and storage. The inset shows the sweat absorption of these materials over 50 h. (E) UV–visible spectroscopy results showing the transmittance of a 1-layer cellulose film and a 2-layers cellulose film. (F) Water contact angle of a sample of TPC at 75°C and room temperature at various times after corona and UV/ozone treatment. (G) Lap shear tests of the bonding between a cellulose film and a substrate of TPC at various conditions. The shaded areas represent 95% confidence intervals across five tests. (H, I) Stress–strain behaviors of sweat microfluidic devices with cellulose sealing layers with and without slits during 3-point bending (H) and tensile (I) tests. The insets show the test setup and the laser-patterned cellulose film design in magenta

As mentioned previously, the process for bonding the TPC to the cellulose via the PSA layer involves surface treatment to overcome the relatively low surface energy of these materials.[54] Figure 3F shows that the contact angle of the unmodified surface of TPC is ~110°. Exposure to a corona discharge and UV-induced ozone renders the surface hydrophilic, which enhances the wetting of the PSA against the TPC surface, thus increasing the contact area and bonding strength.[55] Proper operation of the CBVs requires, however, recovery of the hydrophobic

surface properties of the TPC (Figure S5, Supporting Information). Aging in different environmental conditions (75°C vs. RT, 25% RH) leads to recovery within several hours (Figure 3F). The contact angle of the cellulose laminated PSA is ~103°, also hydrophobic (Figure S6, Supporting Information).

Adhesive lap shear testing of the bond between cellulose and TPC indicates a significant increase in strength after surface treatment (Figure 3G). Appropriate dwell times (e.g., 9 h) during initial contact can also enhance
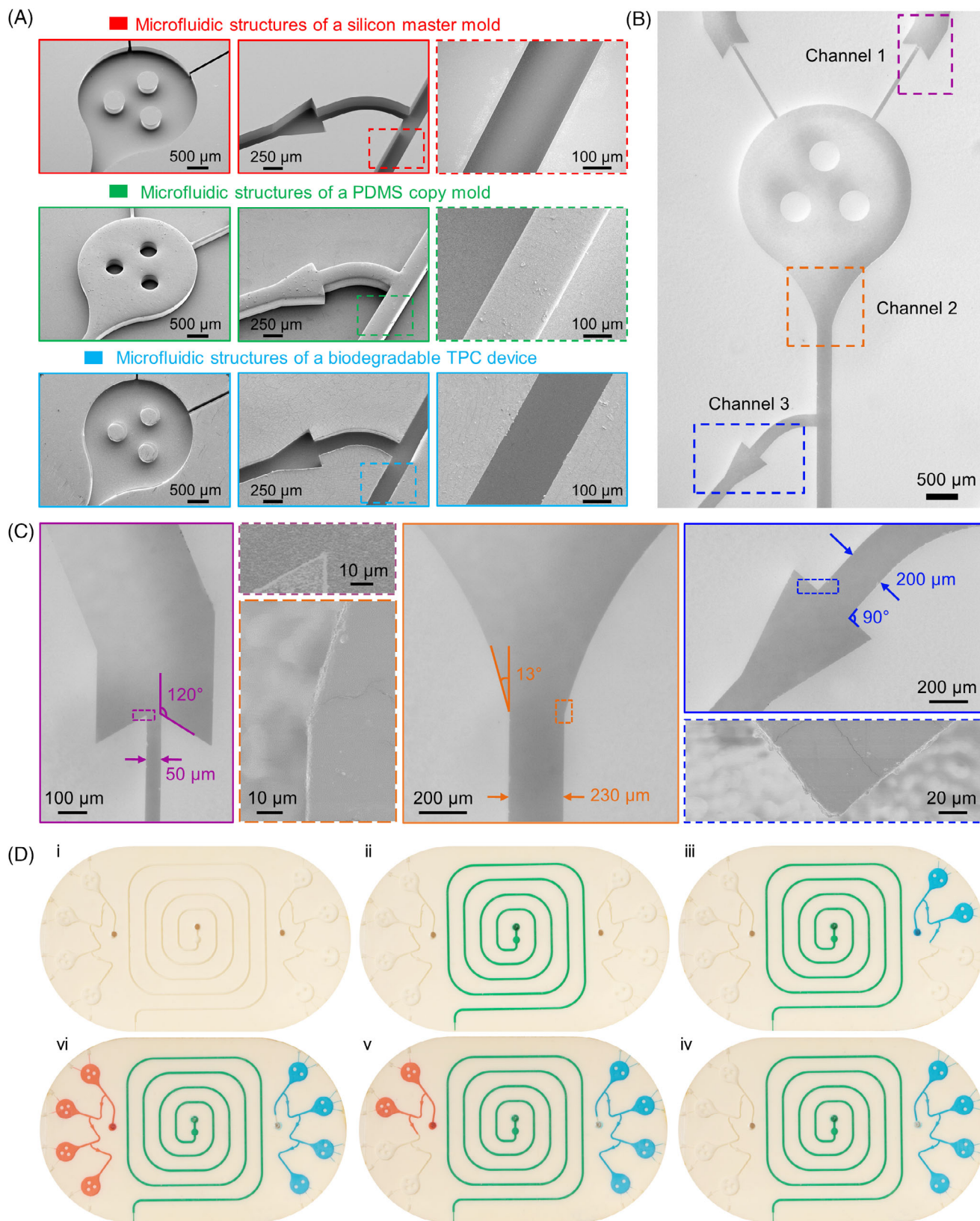
FIGURE 4 Microfluidic structure design and demonstrations of filling guided by capillary bursting valves (CBVs) for chrono-sampling in sequences of reservoirs. (A) Scanning electron micrographs of microfluidic structures on a silicon master mold, a PDMS replica mold, and a layer of TPC. (B, C) Optical images and scanning electron micrographs of three CBVs with indicated channel widths and diverging angles. (D) Optical images demonstrating the working principle of CBVs for chrono-sampling by sequentially filling the channels using dyed artificial sweat. (i) empty device; (ii) filling of the middle microchannel with green dyed artificial sweat; (iii, iv) filling of the microreservoirs on the right with blue dyed artificial sweat guided by capillary bursting valves; (v, vi) filling of the microreservoirs on the left with orange dyed artificial sweat guided by capillary bursting valves

bonding by allowing the adhesive to flow to conform to surface irregularities for improved contact.[56] Increasing the dwell from 9 to 48 h at elevated temperature (75°C) further maximizes the bonding strength (green curve vs. red curve, Figure 3G), but extended times at room temperature can lead to decreases (yellow curve vs. black curve, Figure 3G). The elevated temperature may reduce the viscosity of the PSA and improve its flow. The highest shear strength is achieved when treating the biodegradable TPC with corona and UV/ozone, followed by incubating the bonded assembly at 75°C for 48 h (red curve). The bonding strength remains at room temperature for at least 5 h (blue curve), which is sufficient for maintaining stable adhesion before, during, and after initiation of use. Extending the storage time to 1 week at either 75°C (cyan curve) or room temperature (purple curve) can maintain sufficient bond strength for proper use. The robust bond between the cellulose and TPC ensured reliable operation, without any loss of adhesion, leakage of fluids or other interfacial modes of failure.

Because the cellulose has a much higher elastic modulus than the TPC, this material significantly influences the effective bending and tensile modulus of the devices. Cutting narrow features in the cellulose around the middle microfluidic channel dramatically reduces the ability of the cellulose layer to resist deformations, thus decreasing the effective modulus of the devices, to facilitate comfortable and reliable bonding to the skin. The results of Figure 3H–I show that these features decrease the overall bending modulus by ~13%, and the tensile elastic modulus by ~93%. A magnified view of the setup for the 3-point bending tests and the patterns of cuts in the cellulose layer appear in Figure S7, Supporting Information.

2.4 | Microfluidic structures and capillary bursting valve designs for sequential sampling of sweat

Scanning electron micrographs of the microfluidic structures show that the complex geometries of the silicon master transfer with high fidelity to the PDMS mold, and then to the TPC, with negligible variations in feature dimensions (Figure 4A). The designs of the CBVs follow from consideration of the characteristic bursting pressures (BPs) in rectangular channels given by the Young–Laplace equation.[57] Details of the working mechanisms and calculations appear in Figure S5, Supporting Information. Figure 4B, C show optical images and scanning electron micrographs of three CBVs (labeled channel #1–3) with channel widths and diverging angles indicated. The edges at the exit regions of the

CBVs are sufficiently sharp to eliminate any noticeable effect on the bursting pressures (Figure 4C). Figure 4D illustrates the filling of the middle microchannel (ii) and each set of microchannels and microreservoirs (right: iii-iv; left: v-vi) with dyed artificial sweat. The reservoirs fill sequentially, in an order that follows the bursting pressures, without any mixing or cross-contamination, as expected.

2.5 | Quantitative colorimetric analysis of pH and chloride

Sweat loss, rate, pH, and chloride concentration provide insights into human physiological state, health, and performance, specifically in the context of conditions such as dehydration status, homeostasis regulation, and electrolyte balance.[54,58] Colorimetric methods enable simple, rapid, and in situ analysis of sweat constituents in a manner that bypasses the cost, complexity, and physical bulk associated with electronic measurement schemes. As mentioned previously, assessments of chloride concentration rely on the reagent silver chloranilate dispersed in pHEMA methanolic suspension and drop-cast into the microreservoirs. Reaction with chloride in sweat produces distinct changes in color that correlate with chloride concentration across a physiologically relevant range for sweat.[59] Colorimetric measurements of pH rely on reactions of anthocyanin, also mentioned previously, that produce reddish-pink colors in acidic solutions, blue-violet hues in neutral ones, and green to yellow colors in basic conditions.[60] Calibration curves follow from digital images of standard samples corresponding to physiologically relevant levels of chloride (25, 50, 75, and 100 mM) and pH (4.5, 5, 5.5, 6, 6.5, and 7) captured with a Color-Checker as a color balance reference (Figure S9, Supporting Information).

Accurate extraction of small differences in color from these images follows from algorithms based on the CIE-LAB color space, referred to as $L^*a^*b^*$, which represents the lightness of the color (L^*, black at 0 and white at 100), the green-red opponent colors (a^*, negative values toward green and positive values toward red), and the blue-yellow opponent colors (b^*, negative values toward blue and positive values toward yellow). Compared to assessments in the RGB color space (Figure S9B, Supporting Information) this approach provides enhanced reliability in practical scenarios where lighting intensity is not well controlled. Previous work used chroma ($C^* = \sqrt{(a^*)^2 + (b^*)^2}$) as the color analysis parameter for analyzing biomarker concentrations.[61] Differences in color associated with different biomarker concentrations
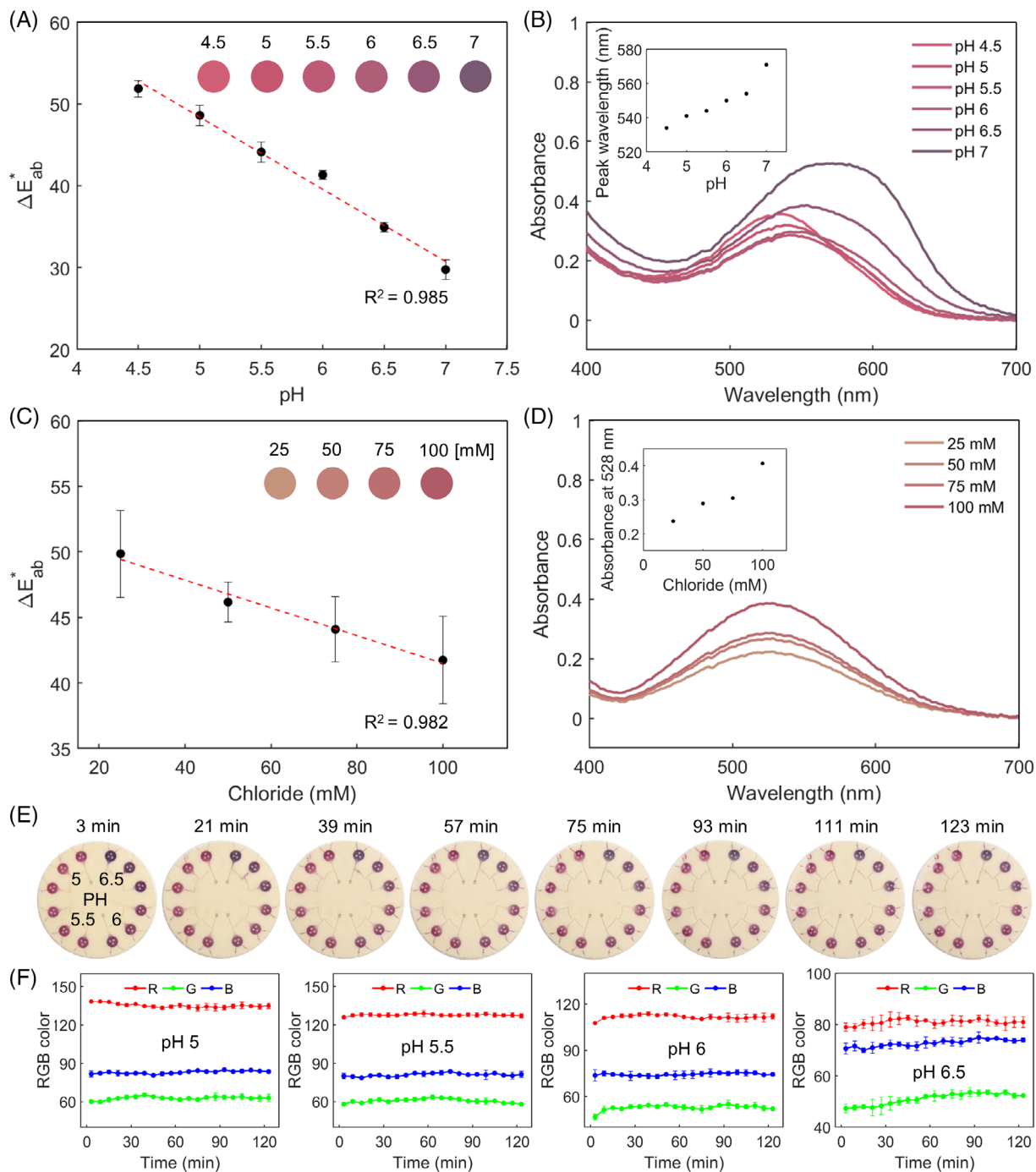
FIGURE 5 Quantitative colorimetric analysis of sweat pH and chloride concentration. (A–D) Standard calibration curves from an image processing algorithm and corresponding ultraviolet (UV)–visible spectroscopy results for various physiologically relevant levels of pH (A, B) and chloride concentration (C, D). The color intensity corresponds to the distance metric ΔE_{ab}^* from the CIELAB color space, plotted as a function of chloride concentration and pH values. The color evolution in the standard calibration curves (A, C) and the presented color for each spectrum (B, D) correspond to the color exhibited at the detection reservoir in the device. The error bars in (A, C) represent one standard deviation of the three measurements of chloride concentrations or pH values corresponding to each standard level. (E, F) Colorimetric analysis of pH assay response as a function of time. Optical images of a device with 4 inlets (E) and extracted, averaged RGB color information at certain time points (F) during a 2-h period after the introduction of pH standard solutions with various pH values (5, 5.5, 6, and 6.5 for each group of reservoirs)

are, however, not only affected by the chromatic colors (a^*, b^*) but also the overall lightness (L^*). Upon saturation, especially at low concentrations, the chromatic color remains constant and most of the changes in color result from changes in lightness. A metric that captures both chromatic colors and lightness is ΔE_{ab}^* (Equation 1):

$$\Delta E_{ab}^* = \sqrt{\left(L_n^* - L_0^*\right)^2 + \left(a_n^* - a_0^*\right)^2 + \left(b_n^* - b_0^*\right)^2} \quad (1)$$

as the distance between the measured point (L_n^*, a_n^*, b_n^*) and the background point (L_0^*, a_0^*, b_0^*).

Figure 5A shows standard calibration curves and corresponding results of ultraviolet–visible spectroscopy (UV–vis) for pH (A, B) and chloride (C, D). The value of ΔE_{ab}^* depends on the chloride concentration and pH. As lightness values can be affected by shadows or other non-ideal illumination conditions, calculations of ΔE_{ab}^* follow after compensation for the background (Figure S10, Supporting Information), as described in the Experimental Section. The resulting ΔE_{ab}^* values decrease linearly with increasing pH ($R^2 = 0.985$) and chloride concentration ($R^2 = 0.999$). Details appear in Figure S11–12, the Supporting Information, and the Experimental Section. The UV–vis results show similar trends. Furthermore, color information from the pH detection reservoirs (Figure 5E, F) during a 2-h period after the introduction of pH standard solutions (5, 5.5, 6, and 6.5 for each group of reservoirs) for a device with four separate inlets indicates that the color responses stabilize in about 15 min. Previous work demonstrates that the chloride assay develops color in less than 3 min.[9]

2.6 | Sweat collection, biomarker detection, and in situ chrono-sampling in human trials

Figure 6 summarizes examples of using these biodegradable sweat microfluidic systems in trials with human subjects, for mounting on the upper arm and chest while running on a treadmill and resting in a sauna (Figure 6A). The experiments involve the chest and the upper arm, simply as two representative convenient locations for mounting. Data acquisition involves digital image capture with a smartphone. Automated algorithms extract CIE-LAB color values from the images, perform background calibration, and then convert the color values to pH and chloride concentration, without the need for color reference markers used in previous work.[8,51]

Figure 6B shows a photograph of a subject wearing a sweat microfluidic device while running on a treadmill. Figure 6C, D present images of devices on subject #1 during exercise (C) and sauna exposure (D) at various times during the study. The results for subject #2 appear in Figure S13, Supporting Information. Subjects reported no sense of discomfort or limitation in body movement. The position of the filling front of the middle microchannel, along with its characteristic dimensions, determines the sweat loss as a function of time and the average sweat

rates for the region of the skin that aligns with the opening in the skin adhesive and corresponding inlet at the base of the device. The colors in the reservoirs define the pH and chloride concentration. Figure 6E, F show the sweat loss as a function of time measured from subject #1 during exercise (E) and sauna exposure (F). For this subject, running on a treadmill typically initiates sweating after ~15 min and continues until all of the reservoirs fill within ~30 min. Sitting in a sauna requires ~30 min to initiate sweating, and complete filling occurs ~55 min. As physiological sweat rates range from 12 to 120 µl h^{-1} cm^{-2},[62] with a sweat collection area of 60 mm^2 (corresponding to ~60 sweat glands in upper arm and ~12 sweat glands in chest),[63,64] the sweat rate is expected to be from 0.12 to 1.2 µl/min. The average sweat rate measured in the study is 0.97 µl/min during exercise and 0.22 µl/min in the sauna. Referring to a form of Poiseuille's law as described elsewhere,[10] for channels with dimensions of 330 µm in depth, 300 µm in width, and ~200 mm in length, the flow rate of sweat through the microfluidic channel for monitoring sweat rate/loss is 174.6 µl/min at an applied pressure of 2 kPa, a physiologically relevant pressure for sweat glands.[9] This rate is significantly greater than the measured sweat rate in these studies, indicating a negligible effect of backpressure and fluidic drag on flow of sweat into the device.

Measurements of concentrations of chloride (Figure 6G) in this sequence of microreservoirs indicate that the average concentrations are 27 ± 2.5 mM (reservoir #1, ~18 min) and 33 ± 2.4 mM (reservoir #3, ~24 min) in exercise, 37 ± 0.1 mM (reservoir #1, ~49 min) and 39 ± 3 mM (reservoir #2, ~52 min) in sauna exposure. The average chloride concentrations (~30 ± 2.5 mM in exercise; ~38 ± 2.4 mM in sauna) are consistent with normal values (10–100 mM).[65] The pH values (Figure 6H) show little dependence on time for both exercise (5.2 ± 0.1; reservoirs #1–#3) and sauna exposure (5.2 ± 0.1; reservoirs #1-#3). The average pH values are within the typical range (4.7–6.6)[66] and the absence of time dependence is consistent with previously published studies.[67–69] Although the #4 reservoirs were filled for both exercise and sauna exposure, due to insufficient time for the pH colorimetric assays to stabilize before the bursting of all the valves, only the pH values in the first 3 reservoirs were evaluated (Figure 6H). Designs that involve only a single outlet channel positioned after the last reservoir avoid this limitation.

Compared with sauna exposure, exercise induces a higher average sweat rate, lower chloride concentrations, and negligible pH variations (Figure 6I). Previous literature shows the reduction of skin temperature during exercise, which is most likely due to vasoconstriction.[70] Thermal exposure, on the other hand, increases the skin
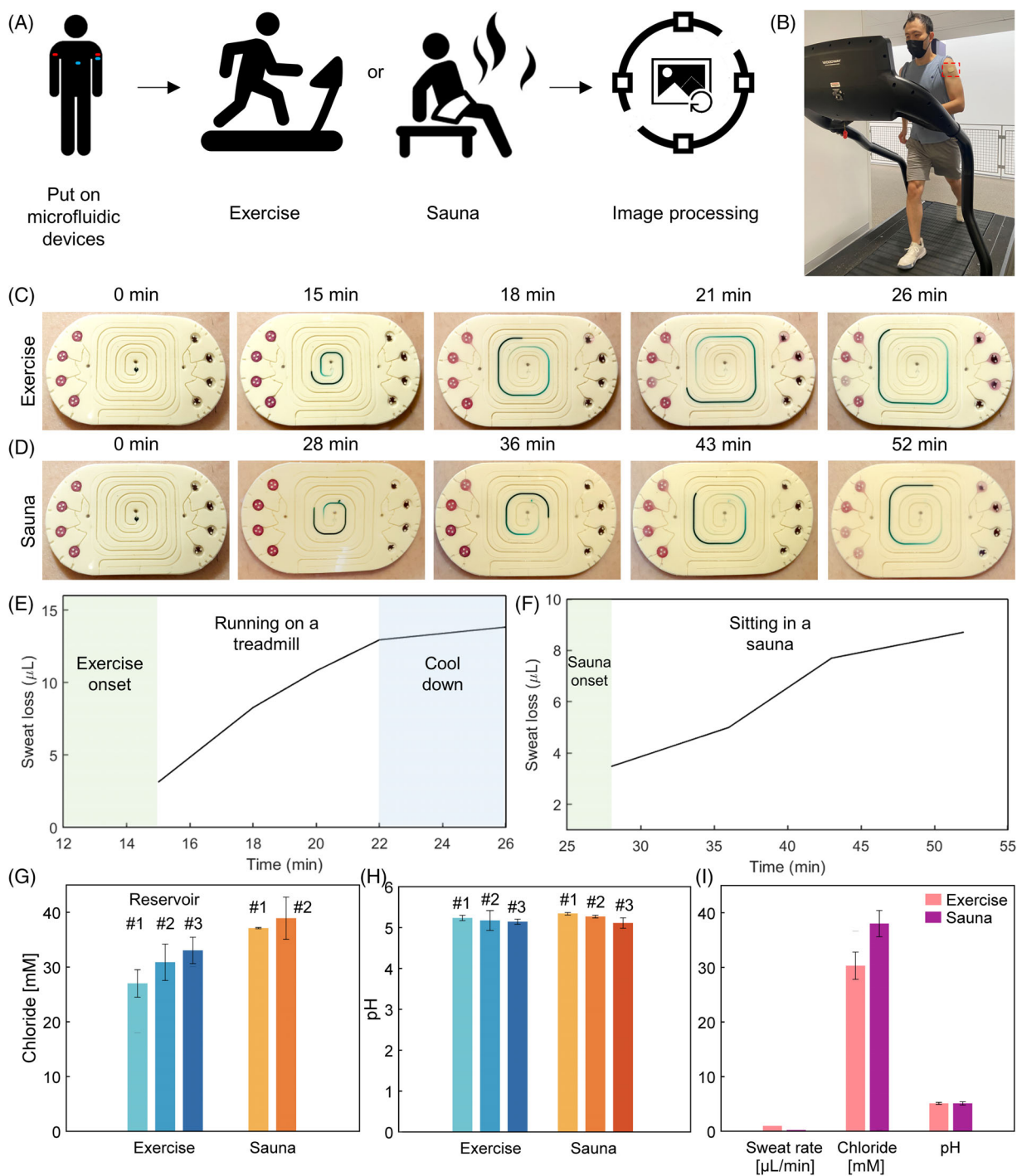
FIGURE 6 Human trials during physical exercise and thermal exposure. (A) Schematic illustration indicating the sequence of procedures for human trials and data capture. (B) Photograph of a subject wearing a sweat microfluidic device on the upper arm during running on a treadmill run. Images of sweat microfluidic devices applied to subject #1 during exercise (C) and sauna exposure (D) at various times during the study. Sweat loss as a function of time measured from subject #1 during exercise (E) and sauna exposure (F). Chloride concentration (G) and pH value (H) corresponding to each reservoir obtained by colorimetric image processing. (I) Comparison of average sweat rate (0.97 μl/min vs. 0.22 μl/min), chloride concentration (30 ± 2.5 mM vs. 38 ± 2.4 mM), and pH level (5.2 ± 0.1 vs. 5.2 ± 0.1) during exercise and sauna exposure. The error bars represent one standard deviation across three measured chloride concentrations or pH values in each reservoir

temperature to close to 40°C.[71–73] The higher chloride concentrations in sauna sweat are consistent with previously reported results that suggest that sweat chloride increases with increasing skin temperature.[74,75] The lower chloride concentrations in exercise sweat could also be the result of dilution effect caused by greater sweat production.[76] The chloride assay does not show significant temperature dependence in its response over a

range relevant to the surface of the skin.[77] Data collected from subject #2 shows similar trends (Figure S13, Supporting Information).

3 | CONCLUSIONS

This paper introduces a collection of biodegradable materials, fabrication methods, assembly techniques, design schemes, and device architectures for soft, skin-interfaced microfluidic systems capable of monitoring sweat loss, sweat rate, pH, and chloride concentration. The technology exploits a thermoplastic copolyester elastomer for the microfluidic layer, a cellulose film and pressure sensitive adhesive as a sealing layer, and carefully selected chemical reagents as colorimetric assays. The resulting platforms can fully degrade in natural soil or composting facilities to organic compounds that can act as plant nutrients, thereby eliminating environmental stresses from discarded devices. The mechanical, chemical, optical, and thermal properties of these biodegradable materials are well suited for these applications, as an alternative to previously reported non-degradable options. The multi-step soft lithography fabrication process yields high-precision surface relief structures for rapid prototyping of intricate microfluidic architectures. Human subject trials during both treadmill exercises and sauna exposures demonstrate the ability of these devices to track sweat rate, sweat loss, and provide colorimetric readout of pH and chloride concentration without loss of adhesion, leakage of fluids, or other modes of failure, thus obtaining information on dehydration status, homeostasis regulation, and electrolyte balance.

The use of a commercially available thermoplastic material as the microfluidic layer offers process compatibility with scalable manufacturing methods such as injection molding for mass production. The selected biodegradable constituent materials and corresponding fabrication techniques can easily be adopted or modified by researchers or by companies to build other types of wearable platforms with superior biodegradability. Additional work will focus on optimizing and automating the entire process, as the basis for continuous manufacturing of standardized devices on an industrial scale using low-energy and low-cost methods. Other future directions are in the development of additional biodegradable colorimetric chemistries for assessments of other important biomarkers in sweat. The simplicity of these wearable devices in terms of both usage and manufacturing, and more importantly, their capabilities to biodegrade in a short period of time to help mitigate environmental issues suggest prospects for wide-spread, personalized devices for health monitoring in hospital and home settings alike.

4 | EXPERIMENTAL SECTION

4.1 | Fabrication of microfluidic molds

Spin coating KMPR 1010 (MicroChem, MA, USA) at 3000 RPM for 30 s formed a ~10 μm-thick layer of negative photoresist on a silicon wafer (4-inch diameter; 2 mm thick). Soft baking on a hot plate for 5 min, exposing to a laser maskless aligner (Heidelberg MLA150) with a 375 nm diode laser beam at 3700 mJ cm^{-2} for 30 min, hard baking for 5 min, and then developing in AZ917MIF for 5 min created patterns of photoresist in geometries to define the microfluidic structures. Deep reactive-ion etching (DRIE) created trenches in the exposed regions of the silicon wafer to a depth of 330 μm (STS Pegasus ICP-DRIE; SPTS Technologies Ltd.). A profilometer (Dektak 8) confirmed the depth of the microchannels. The last step in the DRIE process formed a thin film of polytetrafluoroethylene (PTFE) to facilitate release of cured PDMS molds via processes of soft lithography. Subsequently, placing the silicon master mold into a laser-cut acrylic container, pouring a mixture of white dye (Reynolds Advanced Material, IL, USA, 5 wt%) and PDMS precursor (10:1 base to curing agent; Sylgard 184, Dow Corning, MI, USA), followed by degassing in a desiccator for 30 min and curing for 5 h at 75°C yielded a PDMS replica mold.

4.2 | Fabrication of TPC microfluidic layers

Pre-drying biodegradable TPC pellets in air at 85°C for 2 h and storing the material in a desiccator cabinet at RT, 20% RH eliminated water absorption that can otherwise occur during exposure to the ambient environment before processing. Melting pellets at 160°C on a stainless steel plate for 10 min, applying a 0.5 MPa pressure for 5 min using a hydraulic press (Carver, Inc.), and then releasing the pressure and cooling the assembly to room temperature created a 1 mm-thick TPC film. A shim used during this process defined the thickness. Placing the film on a PDMS mold, pressing with a stainless steel plate, and then heating at 160°C for 4 h allowed the TPC film to soften and slowly fill into the microfeatures of relief on the surface of the PDMS. A 0.5 mm-thick shim placed on the PDMS mold defined the device thickness.

A CO_2 laser system (Universal Laser Systems VLS 2.30, 30 W, 10.6 μm) cut the resulting piece of TPC into an oval shape to define the overall outline of the device. A mechanical punch tool defined 1 mm diameter holes through the TPC, as inlets for sweat to pass from the skin into the sealed microfluidic structure.

4.3 | Development of colorimetric assays for chloride and pH

Suspending 150 mg of red cabbage powder in 5 ml of deionized (DI) water yielded the colorimetric pH assay solution. Drop casting 0.9 µl of this solution onto filter papers (Sigma Aldrich, MO, USA) placed in the microreservoirs, drying in a desiccator for 10 min, drop casting another 0.9 µl and drying for another 15 min completed the pH assays. The three posts in the reservoirs prevent mechanical collapse that might otherwise occur upon impact or application of pressure. The colorimetric chloride assay solution consisted of 50 mg of silver chloranilate (Green Room Board CO., NC, USA) dispersed in 200 ml of 2 wt% polyhydroxyethylmethacrylate (Sigma-Aldrich, MO, USA) methanolic suspension. Vortexing the solution immediately before application ensured a uniform suspension. Drop casting delivered 0.3 µl of the assay into the microreservoirs for chloride sensing. The two posts in the reservoirs prevent mechanical collapse while preventing air bubble trapping during sweat flow.

4.4 | Processes for assembling microfluidic devices

A picosecond laser micromachining system (Protolaser R4, LPKF, 8 W, 515 nm, 1.5 ps) formed slits in films of cellulose. Exposing the TPC to a corona discharge (SpotTEC; Tantec) for 1 min, followed by exposing both the TPC and the laser-patterned cellulose film to UV/ozone (UVO; Jelight Model 144A) for 5 min, and finally exposing the TPC layer to corona again for 1 min enhanced the surface energy of the films and prepared them for bonding. Laminating the cellulose film with the acrylic PSA facing the TPC layer, pressing onto the assembly for 10 s, and then incubating at 75°C for 48 h led to strong bonding and a robust, sealed microfluidic system. Corona treating the bottom of the TPC layer for 30 s enabled strong bonding of the laser-patterned skin-compatible adhesive (PC2723U, Scapa Healthcare).

4.5 | Finite-element analysis of devices under mechanical loading

3D FEA with the commercial software Abaqus enabled evaluation of the mechanical response of devices mounted on skin phantoms (2.5 mm-think, 130 kPa) to stretching, bending, and twisting. The results included deformed configurations and strain distributions under different levels and types of loading. Eight-node 3D solid elements were chosen for the TPC and skin phantoms, and four-node shell elements for the cellulose. The TPC and the skin phantom were modeled as incompressible elastomeric materials with Mooney-Rivlin hyperelastic behavior and elastic moduli $E_{TPC} = 5.3$ MPa and $E_{Skin-phantom} = 130$ kPa, respectively. The cellulose was modeled with linear elastic behavior and an elastic modulus $E_{Cellulose} = 1.75$ GPa and Poisson's ratio $\nu_{Cellulose} = 0.39$. For stretching, displacements corresponding to 25% stretching were applied to the ends of the skin phantom. For bending, the bottom surface of the skin phantom was pressed against a rigid cylinder of 35 mm radius. For twisting, the two ends of the skin phantom were twisted by 90° relatively.

4.6 | Characterization of mechanical properties

Tensile testing (Mark-10) of TPC samples in dogbone geometries (ASTM D638) and cellulose samples in rectangular shapes (ASTM D882) yielded stress/strain relationship for strains from 0% to 600% and 0% to 20%, respectively. The strain rate was 10 mm/min. A linear fit of data for strains from 0% to 18%, and 0% to 1.5% determined Young's modulus of these two materials, respectively. Cyclic testing of TPC samples at various strains (5%, 10%, 15%, 20%, and 30%) and 0.5 mm/min yielded the yield strains. The materials experienced 5 cycles at each strain. Tensile (Mark-10) and 3-point bending (DMA; TA Instruments RSA G2) tests of microfluidic devices constructed using cellulose layers with and without slits yielded the tensile elastic moduli and bending moduli, respectively. The results confirmed the effectiveness of the laser-patterned cellulose layer. In the tensile tests, the devices were stretched at 0.5 mm/min until failure of the adhesive bonding between the TPC and the cellulose layer. In the 3-point bending tests, the middle parts of the devices were pressed to reach a displacement of 5 mm. Strips of TPC and cellulose were bonded with a 12 mm × 12 mm overlapping area using different processing conditions and fixed to aluminum plates. Applying tensile forces at both ends and dividing the forces by the overlapping areas yielded the lap shear strengths.

4.7 | Measurements of absorption and barrier properties

Measuring the change in weight of bulk samples of cellulose, TPC and PDMS (control group) submerged in artificial sweat yielded data on the sweat absorption rate. The samples were stored at room temperature in capped scintillation vials filled with artificial sweat (Stabilized Artificial

Eccrine Perspiration; Pickering Laboratories), removed periodically, gently dried of surface water (using Kim Wipes), and weighed on a microbalance. Measuring the change in weight of a PDMS container filled with a cylinder of hydrogel and fixed onto a glass slide using epoxy with a capping layer of a film under test defined the water vapor permeability. The films evaluated in this way included PDMS (∼50 μmt thickness), cellulose (∼45 μm and ∼ 90 μm thicknesses). Each sample was weighed on a microbalance every few hours until the weight was stabilized.

4.8 | Characterization of optical properties

A UV–vis spectrophotometer (LAMBDA 1050; Perkin Elmer) enabled transmittance measurements of cellulose films in a range of wavelengths from 200 to 800 nm. A different UV–vis spectrophotometer (Nanodrop 2000; ThermoFisher) yielded absorbance measurements of pH and chloride standard solutions at various physiologically relevant levels in a range of wavelengths from 400 to 700 nm. Each measurement used 2 μl of assay solutions.

4.9 | Characterization of thermal properties

Differential scanning calorimetry (Netzsch) enabled measurements of the thermal properties of the TPC. Samples (5 mm × 2 mm) were heated in an aluminum pan from −80 to 200°C at 10°C/min in a carrying gas atmosphere of nitrogen, flowing at 50 ml/min. An empty aluminum pan served as the reference. Heat flow data were collected for each experiment, and the baseline signal was subtracted from an empty sample experiment performed immediately prior.

4.10 | Measurements of contact angle

Samples for contact angle measurements included untreated TPC films, and TPC films after exposure to a corona discharge (SpotTEC; Tantec) for 1 min, UVO (UVO; Jelight Model 144A) for 5 min, and corona again for 1 min, followed by aging at different environmental conditions (75°C vs. RT, 25% RH) for various times. A contact angle goniometer (VCA-Optima XE, MA, USA) enabled static contact angle measurements of DI water. An automated dispenser produced 0.5 μl drops of water for these measurements.

4.11 | Image acquisition

A digital optical microscope (VHX-5000, KEYENCE, Osaka, Japan) and a scanning electron microscope (SEM, EPIC Hitachi SU8030, Tokyo, Japan) produced micrographs of the devices.

4.12 | Color analysis and image processing algorithm

Calibration curves were determined from digital images of standard samples corresponding to physiologically relevant levels of chloride (25 , 50, 75, and 100 mM) and pH (4.5, 5, 5.5, 6, 6.5, and 7) with a 24-color card (X-rite ColorChecker Classic Nano) for color correction. A DSLR camera (Canon 90D) served as an imaging tool for capturing the images. The processing algorithm first extracted the CIELAB color values from the images, then performed a background calibration, and finally converted the calibrated color values to pH and chloride concentrations. For background calibration, brightness values of the device at regions near the reservoirs were measured as a function of the coordinates along a line. Each line of the measured background was fit to a linear form using the least-squares method. The resulting linear curves were then subtracted from the background and the reservoir brightness values to obtain constant background brightness values. After background calibration, ΔE_{ab}^* values were calculated from each reservoir to define the standard calibration curves.

4.13 | Human trials

Testing involved two healthy, consenting adults as volunteers. The mounting locations (upper arm, forearm, or chest) were cleaned with an alcohol gauze pad before attaching the biodegradable microfluidic devices. Subjects ran on a treadmill for ∼30 min or rested in a portable sauna for ∼55 min. The studies were conducted on different days. Digital images were captured using smartphone cameras every few minutes during the trials for sweat loss/rate calculations and colorimetric analyses. The CIELAB color values from each reservoir were extracted from the images. After background calibration, the calibrated color values were converted to the pH and chloride concentrations.

AUTHOR CONTRIBUTIONS
S.L. and J.A.R. conceived the concepts, designed the experiments, interpreted the results, and wrote the paper. S.L. led the experimental work with support from D.S.Y., S.W., and Y.S. D.S.Y. performed the colorimetric analysis.

CONFLICT OF INTEREST

J.A.R. is a co-founder of a company, Epicore Biosystems, that makes and sells non-degradable microfluidic devices for sweat analysis.

ORCID

John A. Rogers https://orcid.org/0000-0002-2980-3961

REFERENCES

1. Kim D-H, Lu N, Ma R, et al. Epidermal Electronics. *Science*. 2011;333(6044):838-843. doi:10.1126/science.1206157
2. Choi J, Ghaffari R, Baker LB, Rogers JA. Skin-interfaced systems for sweat collection and analytics. *Science Advances*. 2018;4((2)):eaar3921. doi:10.1126/sciadv.aar3921
3. Ghaffari R, Choi J, Raj MS, et al. Soft wearable systems for colorimetric and electrochemical analysis of biofluids. *Adv Funct Mater*. 2020;30(37):1907269. doi:10.1002/adfm.201907269
4. Moretto H-H, Schulze M, Wagner G. *Ullmann's Encyclopedia of Industrial Chemistry*. John Wiley & Sons, Ltd; 2000.
5. Miranda I, Souza A, Sousa P, et al. Properties and applications of PDMS for biomedical engineering: a review. *J Funct Biomater*. 2022;13(1):2.
6. Bélanger M, Marois Y. Hemocompatibility, biocompatibility, inflammatory andin vivostudies of primary reference materials low-density polyethylene and polydimethylsiloxane: a review. *J Biomed Mater Res*. 2001;58(5):467-477. doi:10.1002/jbm.1043
7. Epicore Biosystems. https://www.epicorebiosystems.com/
8. Zhang Y, Guo H, Kim SB, et al. Passive sweat collection and colorimetric analysis of biomarkers relevant to kidney disorders using a soft microfluidic system. *Lab Chip*. 2019;19(9):1545-1555. doi:10.1039/C9LC00103D
9. Choi J, Bandodkar AJ, Reeder JT, et al. Soft, skin-integrated multifunctional microfluidic systems for accurate colorimetric analysis of sweat biomarkers and temperature. *ACS Sens*. 2019;4(2):379-388. doi:10.1021/acssensors.8b01218

10. Reeder JT, Choi J, Xue Y, et al. Waterproof, electronics-enabled, epidermal microfluidic devices for sweat collection, biomarker analysis, and thermography in aquatic settings. *Sci Adv*. 2019;5(1):eaau6356. doi:10.1126/sciadv.aau6356
11. Heaton JW, Marangoni AG. Chlorophyll degradation in processed foods and senescent plant tissues. *Trends Food Sci Technol*. 1996;7(1):8-15. doi:10.1016/0924-2244(96)81352-5
12. Kräutler B. Breakdown of chlorophyll in higher plants-Phyllobilins as abundant, yet hardly visible signs of ripening, senescence, and cell death. *Angew Chem Int Ed*. 2016;55(16):4882-4907. doi:10.1002/anie.201508928
13. Rodriguez-Amaya DB. Natural food pigments and colorants. *Curr Opin Food Sci*. 2016;7:20-26. doi:10.1016/j.cofs.2015.08.004
14. Marszałek K, Woźniak Ł, Kruszewski B, Skąpska S. The effect of high pressure techniques on the stability of anthocyanins in fruit and vegetables. *Int J Mol Sci*. 2017;18(2):277. doi:10.3390/ijms18020277
15. Ghareaghajlou N, Hallaj-Nezhadi S, Ghasempour Z. Red cabbage anthocyanins: stability, extraction, biological activities and applications in food systems. *Food Chem*. 2021;365:130482. doi:10.1016/j.foodchem.2021.130482
16. Sri Sruthi P, Balasubramanian S, Senthil Kumar P, et al. Eco-friendly pH detecting paper-based analytical device: towards process intensification. *Anal Chim Acta*. 2021;1182:338953. doi:10.1016/j.aca.2021.338953
17. Zare M, Bigham A, Zare M, Luo H, Rezvani Ghomi E, Ramakrishna S. pHEMA: an overview for biomedical applications. *Int J Mol Sci*. 2021;22(12):6376. doi:10.3390/ijms22126376
18. Mabilleau G, Moreau MF, Filmon R, Baslé MF, Chappard D. Biodegradability of poly (2-hydroxyethyl methacrylate) in the presence of the J774.2 macrophage cell line. *Biomaterials*. 2004;25(21):5155-5162. doi:10.1016/j.biomaterials.2003.12.026
19. Bonifácio VG, Figueiredo-Filho LC, Marcolino LH, Fatibello-Filho O. An improved flow system for chloride determination in natural waters exploiting solid-phase reactor and long path-length spectrophotometry. *Talanta*. 2007;72(2):663-667. doi:10.1016/j.talanta.2006.11.036
20. Song JH, Murphy RJ, Narayan R, Davies GBH. Biodegradable and compostable alternatives to conventional plastics. *Philos Trans Royal Soc B Biol Sci*. 2009;364(1526):2127-2139. doi:10.1098/rstb.2008.0289
21. Choi J, Kang D, Han S, Kim SB, Rogers JA. Thin, soft, skin-mounted microfluidic networks with capillary bursting valves for Chrono-sampling of sweat. *Adv Healthc Mater*. 2017;6(5):1601355. doi:10.1002/adhm.201601355
22. Lee CH, Ma Y, Jang K-I, et al. Soft core/shell packages for stretchable electronics. *Adv Funct Mater*. 2015;25(24):3698-3704. doi:10.1002/adfm.201501086
23. Kim D-H, Viventi J, Amsden JJ, et al. Dissolvable films of silk fibroin for ultrathin conformal bio-integrated electronics. *Nature Mater*. 2010;9(6):511-517. doi:10.1038/nmat2745
24. Hwang S-W, Tao H, Kim D-H, et al. A physically transient form of silicon electronics. *Science*. 2012;337(6102):1640-1644. doi:10.1126/science.1226325
25. Won SM, Koo J, Crawford KE, et al. Natural wax for transient electronics. *Adv Funct Mater*. 2018;28(32):1801819. doi:10.1002/adfm.201801819
26. Kim SH, Lee HJ, Yoo J-C, et al. Novel transparent collagen film patch derived from duck's feet for tympanic membrane perforation. *J Biol Sci Polym Edi*. 2018;29(7-9):997-1010. doi:10.1080/09205063.2017.1374031

27. Hwang S-W, Song J-K, Huang X, et al. High-performance biodegradable/transient electronics on biodegradable polymers. *Adv Mater.* 2014;26(23):3905-3911. doi:10.1002/adma.201306050

28. Yu KJ, Kuzum D, Hwang S-W, et al. Bioresorbable silicon electronics for transient spatiotemporal mapping of electrical activity from the cerebral cortex. *Nature Mater.* 2016;15(7):782-791. doi:10.1038/nmat4624

29. Kang S-K, Murphy RKJ, Hwang S-W, et al. Bioresorbable silicon electronic sensors for the brain. *Nature.* 2016;530(4):71-76. doi:10.1038/nature16492

30. Luo M, Martinez AW, Song C, Herrault F, Allen MG. A microfabricated wireless RF pressure sensor made completely of biodegradable materials. *J Microelectromech Syst.* 2014;23(1):4-13. doi:10.1109/JMEMS.2013.2290111

31. Tsang M, Armutlulu A, Martinez AW, Allen SAB, Allen MG. Biodegradable magnesium/iron batteries with polycaprolactone encapsulation: A microfabricated power source for transient implantable devices. *Microsyst Nanoeng.* 2015;1(1):1.

32. Hwang S-W, Lee CH, Cheng H, et al. Biodegradable elastomers and silicon Nanomembranes/nanoribbons for stretchable, transient electronics, and biosensors. *Nano Lett.* 2015;15(5):2801-2808. doi:10.1021/nl503997m

33. Gross RA, Kalra B. Biodegradable polymers for the environment. *Science.* 2002;297(5582):803-807. doi:10.1126/science.297.5582.803

34. Farmer N. *Trends in Packaging of Food, Beverages and Other Fast-Moving Consumer Goods (FMCG): Markets, Materials and Technologies.* Elsevier; 2013. doi:10.1533/9780857098979

35. Bastioli C. Properties and applications of mater-bi starch-based materials. *Polym Degrad Stab.* 1998;59(1):263-272. doi:10.1016/S0141-3910(97)00156-0

36. Smith R. *Biodegradable Polymers for Industrial Applications.* Elsevier; 2005. doi:10.1533/9781845690762

37. Platt DK, Limited RT. *Biodegradable Polymers: Market Report.* ISmithers Rapra Publishing; 2006.

38. Plackett D, Siró I. In: Lagarón J-M, ed. *Multifunctional and Nanoreinforced Polymers for Food Packaging.* Woodhead Publishing; 2011:498-526.

39. Byun Y, Kim YT. In: Han JH, ed. *Innovations in Food Packaging.* 2nd ed. San Diego: Academic Press; 2014:369-390.

40. Laftah WA. Influence of plant natural fibers on polymer hydrogel properties: A short review. *Int J Eng Res Technol.* 2017;6(7):46-51.

41. de Matos Costa AR, Crocitti A, Hecker de Carvalho L, Carroccio SC, Cerruti P, Santagata G. Properties of biodegradable films based on poly(butylene succinate) (PBS) and poly(butylene Adipate-co-terephthalate) (PBAT) blends. *Polymers.* 2020;12(10):2317. doi:10.3390/polym12102317

42. APINAT™ BIO biodegradable TPC compounds. Plastics products. Trinseo. https://www.trinseo.com/products/plastics/products/bioplastics/apinat-bio.

43. Satti SM, Shah AA. Polyester-based biodegradable plastics: an approach towards sustainable development. *Lett Appl Microbiol.* 2020;70(6):413.

44. Zhanqi G, Shaogui Y, Na T, Cheng S. Microwave assisted rapid and complete degradation of atrazine using TiO$_2$ nanotube photocatalyst suspensions. *J Hazard Mater.* 2007;145(2):424-430. doi:10.1016/j.jhazmat.2006.11.042

45. Yusoff R, Nguyen LTH, Chiew P, Wang ZM, Ng KW. Comparative differences in the behavior of TiO$_2$ and SiO$_2$ food additives in food ingredient solutions. *J Nanopart Res.* 2018;20(3):76. doi:10.1007/s11051-018-4176-8

46. Tourinho PS, van Gestel CAM, Lofts S, Svendsen C, Soares AMVM, Loureiro S. Metal-based nanoparticles in soil: fate, behavior, and effects on soil invertebrates. *Environ Toxicol Chem.* 2012;31(8):1679-1692. doi:10.1002/etc.1880

47. Swiler DR. *Kirk-Othmer Encyclopedia of Chemical Technology.* John Wiley & Sons, Ltd; 2005.

48. Pérez J, Muñoz-Dorado J, de la Rubia T, Martínez J. Biodegradation and biological treatments of cellulose, hemicellulose and lignin: an overview. *Int Microbiol.* 2002;5(2):53-63. doi:10.1007/s10123-002-0062-3

49. Pathak Navneet VM. Review on the current status of polymer degradation: A microbial approach. *Bioresour Bioprocess.* 2017;4(1):15. doi:10.1186/s40643-017-0145-9

50. Gaytán I, Burelo M, Loza-Tavera H. Current status on the biodegradability of acrylic polymers: microorganisms, enzymes and metabolic pathways involved. *Appl Microbiol Biotechnol.* 2021;105(3):1.

51. Koh A, Kang D, Xue Y, et al. A soft, wearable microfluidic device for the capture, storage, and colorimetric sensing of sweat. *Sci Transl Med.* 2016;8:366ra165.

52. Seok M, Yoon S, Kim M, Cho Y-H. A porous PDMS pulsewave sensor with haircell structures for water vapor transmission rate and signal-to-noise ratio enhancement. *Nanoscale Adv.* 2021;3(16):4843-4850. doi:10.1039/D1NA00180A

53. Ayer JE, Schmitt DR, Mayfield RM. Permeation of water vapor through polymeric films. *J Appl Polym Sci.* 1960;3(7):1-10. doi:10.1002/app.1960.070030701

54. Jin X, Heepe L, Strueben J, Adelung R, Gorb SN, Staubitz A. Challenges and solutions for joining polymer materials. *Macromol Rapid Commun.* 2014;35(18):1551-1570. doi:10.1002/marc.201400200

55. Li L, Tirrell M, Korba GA, Pocius AV. Surface energy and adhesion studies on acrylic pressure sensitive adhesives. *J Adhes.* 2001;76(4):307-334. doi:10.1080/00218460108030724

56. Williams JA, Kauzlarich JJ. Dwell time effect in peeling PSA laminates. *J Adhes.* 2012;88(10):831-847. doi:10.1080/00218464.2012.705664

57. Cho H, Kim H-Y, Kang JY, Kim TS. How the capillary burst microvalve works. *J Colloid Interface Sci.* 2007;306(2):379-385. doi:10.1016/j.jcis.2006.10.077

58. Popkin BM, D'Anci KE, Rosenberg IH. Water, hydration, and health. *Nutr Rev.* 2010;68(8):439-458. doi:10.1111/j.1753-4887.2010.00304.x

59. Barney JE, Bertolacini RJ. Colorimetric determination of chloride with mercuric chloranilate. *Anal Chem.* 1957;29(1):1187-1188. doi:10.1021/ac60128a023

60. Chigurupati N, Saiki L, Gayser C, Dash AK. Evaluation of red cabbage dye as a potential natural color for pharmaceutical use. *Int J Pharm.* 2002;241(2):293-299. doi:10.1016/S0378-5173(02)00246-6

61. Ray TR, Ivanovic M, Curtis PM, et al. Soft, skin-interfaced sweat stickers for cystic fibrosis diagnosis and management. *Sci Transl Med.* 2021;13(587):13.

62. Sato K, Sato F. American journal of physiology-regulatory. *Integrat Comp Physiol.* 1983;245(2):R203-R208. doi:10.1152/ajpregu.1983.245.2.R203

63. Wilke K, Martin A, Terstegen L, Biel SS. A short history of sweat gland biology. *Int J Cosmet Sci.* 2007;29(3):169-179. doi:10.1111/j.1467-2494.2007.00387.x

64. Taylor NA, Machado-Moreira CA. Regional variations in transepidermal water loss, eccrine sweat gland density, sweat secretion rates and electrolyte composition in resting and exercising humans. _Extreme Physiol Med_. 2013;2(3):4. doi:10.1186/2046-7648-2-4

65. Sonner Z, Wilder E, Heikenfeld J, et al. The microfluidics of the eccrine sweat gland, including biomarker partitioning, transport, and biosensing implications. _Biomicrofluidics_. 2015;9(3):31301. doi:10.1063/1.4921039

66. Possanzini L, Decataldo F, Mariani F, et al. Textile sensors platform for the selective and simultaneous detection of chloride ion and pH in sweat. _Sci Rep_. 2020;10(1):17180. doi:10.1038/s41598-020-74337-w

67. Bandodkar AJ, Choi J, Lee SP, et al. Soft, skin-interfaced microfluidic systems with passive galvanic stopwatches for precise chronometric sampling of sweat. _Adv Mater_. 2019;31(32):1902109. doi:10.1002/adma.201902109

68. Xiao G, He J, Qiao Y, et al. Facile and low-cost fabrication of a thread/paper-based wearable system for simultaneous detection of lactate and pH in human sweat. _Adv Fiber Mater_. 2020;2(5):265-278. doi:10.1007/s42765-020-00046-8

69. Cheng C, Li X, Xu G, et al. Battery-free, wireless, and flexible electrochemical patch for in situ analysis of sweat cortisol via near field communication. _Biosens Bioelectron_. 2021;172:112782. doi:10.1016/j.bios.2020.112782

70. Torii M, Yamasaki M, Sasaki T, Nakayama H. Fall in skin temperature of exercising man. _Br J Sports Med_. 1992;26(1):29-32. doi:10.1136/bjsm.26.1.29

71. Hanninen O. The sauna: Stimulating and relaxing. _Phys Ther_. 1986;1(6):179-181. doi:10.1152/physiologyonline.1986.1.6.179

72. Keast ML, Adamo KB. The Finnish sauna bath and its use in patients with cardiovascular disease. _J Cardiopulm Rehabil Prev_. 2000;20(4):225-230. doi:10.1097/00008483-200007000-00002

73. Kwon K, Kim JU, Deng Y, et al. An on-skin platform for wireless monitoring of flow rate, cumulative loss and temperature of sweat in real time. _Nat Electron_. 2021;4(4):1.

74. Prasad AS, Schulert AR, Sandstead HH, Miale A, Farid Z. Zinc, iron, and nitrogen content of sweat in normal and deficient subjects. _J Lab Clin Med_. 1963;62(1):84-89.

75. Stauber JL, Florence TM. A comparative study of copper, lead, cadmium and zinc in human sweat and blood. _Sci Total Environ_. 1988;74:235-247. doi:10.1016/0048-9697(88)90140-4

76. Ohara K. Chloride concentration in sweat; its individual, regional, seasonal and some other variations, and interrelations between them. _Jpn J Physiol_. 1966;16(16):274-290. doi:10.2170/jjphysiol.16.274

77. Florence TM, Farrar YJ. Spectrophotometric determination of chloride at the parts-per-billion level by the mercury(II) thiocyanate method. _Anal Chim Acta_. 1971;54(2):373-377. doi:10.1016/S0003-2670(01)82142-5

SUPPORTING INFORMATION

Additional supporting information can be found online in the Supporting Information section at the end of this article.